ACS NANO
Cite This: ACS Nano 2017, 11, 12509–12518
www.acsnano.org

ARTICLE

Ultrathin N-Doped Mo_2C Nanosheets with Exposed Active Sites as Efficient Electrocatalyst for Hydrogen Evolution Reactions

Jin Jia,[†] Tanli Xiong,[†] Lili Zhao,[‡] Fulei Wang,[‡] Hong Liu,[‡] Renzong Hu,[⊥] Jian Zhou,[§] Weijia Zhou,*[,†] and Shaowei Chen[†,#]

[†]Guangzhou Key Laboratory for Surface Chemistry of Energy Materials, New Energy Research Institute, School of Environment and Energy, South China University of Technology, Guangzhou Higher Education Mega Center, Guangzhou, Guangdong 510006, People's Republic of China

[‡]State Key Laboratory of Crystal Materials, Center of Bio & Micro/Nano Functional Materials, Shandong University, 27 Shandanan Road, Jinan, Shandong 250100, People's Republic of China

[⊥]School of Materials Science and Engineering, South China University of Technology, Guangzhou, Guangdong 510640, People's Republic of China

[§]National Laboratory of Solid State Microstructures and Department of Materials Science and Engineering, Nanjing University, 22 Hankou Road, Nanjing, Jiangsu 210093, People's Republic of China

[#]Department of Chemistry and Biochemistry, University of California, 1156 High Street, Santa Cruz, California 95064, United States

Supporting Information

ABSTRACT: **Probing competent electrocatalysts for hydrogen evolution reaction (HER) of water splitting is one of the most hopeful approaches to confront the energy and environmental crisis. Herein, we highlight ultrathin N-doped Mo_2C nanosheets (N-Mo_2C NSs) in the role of greatly efficient platinum-free-based electrocatalysts for the HER. The transformation of crystal phase and structure between MoO_2 nanosheets with a thickness of ∼1.1 nm and N-Mo_2C NSs with a thickness of ∼1.0 nm is studied in detail. Structural analyses make clear that the surfaces of the N-Mo_2C NSs are absolutely encompassed by apical Mo atoms, hence affording an ideal catalyst prototype to expose the role of Mo atoms for the duration of HER catalysis. Theoretical calculations demonstrate that the nanosheet structure, N doping, and particular crystalline phase of Mo_2C produce more exposed Mo active sites, including Mo atoms on the C plane and doped N atoms. Through detailed electrochemical investigations, N-Mo_2C NSs possess HER activity with an onset potential of −48.3 mV *vs* RHE, Tafel slope of 44.5 mV dec^{-1}, and overpotential of 99 mV *vs* RHE at the cathodic current density of 10 mA cm^{-2} with excellent long-term stability. Lastly, the calcination temperature and dicyandiamide amount can obviously affect the phase transformation and surface structure of molybdenum carbide, resulting in an adjustable HER activity. This synthesis mechanism will facilitate the understanding and optimization of Mo-based electrocatalysts in the energy conversion field.**

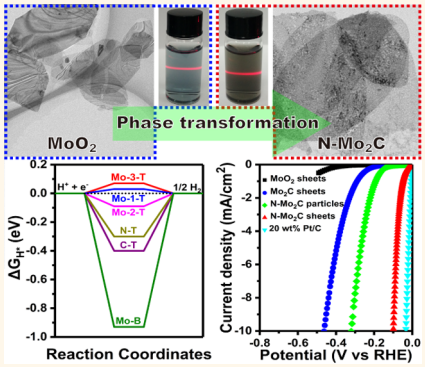

KEYWORDS: *molybdenum carbide, nanosheet, nitrogen doping, density functional theory, hydrogen evolution reaction*

Clean and sustainable hydrogen is deemed to be the most promising energy carrier in the future because of its highest mass-specific energy density and zero emission. Among various hydrogen production processes, electrochemical water splitting is considered an ideal eco-friendly way to produce clean hydrogen energy.[1,2] However, efficient water splitting requires active electrocatalysts for the hydrogen evolution reaction (HER). A platinum (Pt)-based composition, as is well-known, has been utilized as ideal electrocatalysts for the HER process, because of a hydrogen absorption Gibbs free energy (ΔG_{H^*}) of zero.[3−6] However, the high material cost and relative scarcity greatly limit its worldwide applications in the HER process. Therefore, the search for the ideal electrocatalysts for the HER process to

Received: September 17, 2017
Accepted: December 8, 2017
Published: December 8, 2017

DOI: 10.1021/acsnano.7b06607
ACS Nano 2017, 11, 12509–12518

Scheme 1. Theoretical structural models and Gibbs free energy of H* adsorption (ΔG_{H^*}) on various sites of Mo_2C (a, d) and N-Mo_2C (b, c, e). Mo-1-T, Mo-2-T, and Mo-3-T are Mo atoms on the top plane; Mo-B is the Mo atom on the bottom plane; C-T is the C atom on the top plane; N-T is the N atom on the top plane.

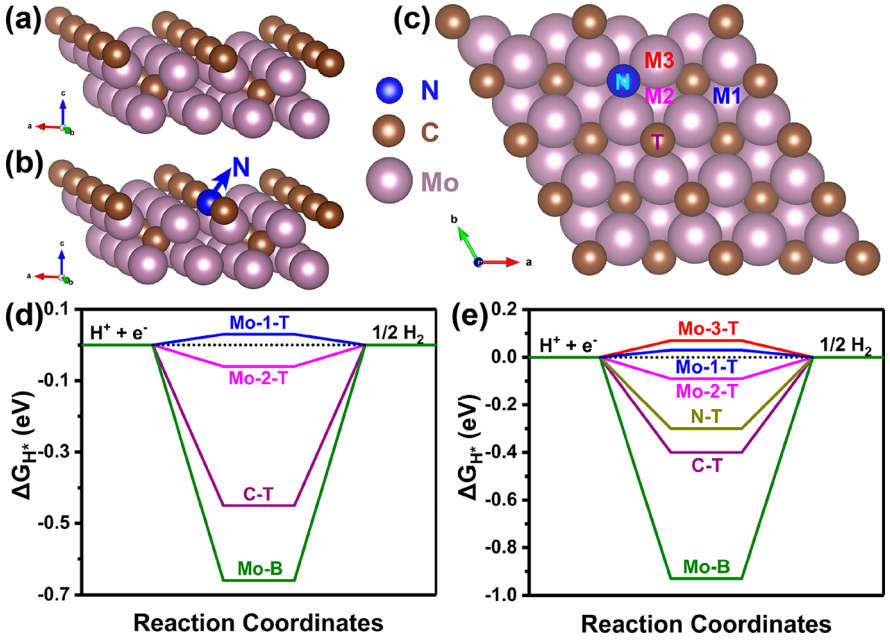

replace Pt-based electrocatalysts is thus highly desirable.[7−10] As an alternative, Mo-based catalysts, such as MoS_2, MoN, Mo_2C, and MoP, have recently received great attention as potential catalysts for HER, due to their cost efficiency, rich molybdenum resources, and favorable activity.[11−19] Among them, molybdenum carbide (Mo_2C), an outstanding early transition-metal carbide, has intensely awakened ever-increasing attention as a high-efficiency HER electrocatalyst with high electrical conductivity and optimal hydrogen-adsorption properties, because the electronic structure of Mo_2C is virtually analogous to that of Pt-group elements.[20−22] It is well-known that the catalytic activities of molybdenum carbide largely hinge on its composition and surface structure and are closely associated with synthesis techniques such as chemical vapor deposition (CVD) and pyrolysis of metal complexes.[23−26] Nevertheless, high-temperature processing usually brings about the coarsening of molybdenum carbide and the excess growth of carbon on the surface of molybdenum carbide, inevitably giving rise to a low density of catalytically active sites. Many efforts have been dedicated to expose more active sites by designing and synthesizing various morphologies of molybdenum carbide, such as nanoparticles,[27] nanowires,[28,29] hierarchical β-Mo_2C nanotubes,[30] vertically aligned nanosheets,[30] cross-linked porous rods,[31] and 2D MXene.[32,33] For instance, nanoporous β-Mo_2C nanowires[25] and MoC_x nano-octahedrons[34] had been recently designed and fabricated by pyrolysis of a MoO_x/amine hybrid precursor and metal−organic frameworks (MOFs) comprising molybdenum-based polyoxometalates (NENU-5), respectively. Despite these developments, owing to the lack of appropriate precursors incorporating uniformly hybridized molybdenum and carbon sources in well-organized nanostructures, the controllable preparation of two-dimensional (2D) molybdenum carbide nanocatalysts is still highly challenging.

Like graphene, 2D crystals are indispensable for exploring the original physical and chemical properties in the dimension limit and for numerous practical and even attractive applications.[35−37] Kang and Ren *et al.*[26] reported the preparation method of large-area and high-quality 2D ultrathin Mo_2C crystals by CVD with CH_4 as the C source, a Mo foil as Mo source, and a Cu foil as the substrate at a high temperature of 1085 °C. However, the above synthesis process of Mo_2C sheets was complicated and had a low yield rate, which was difficult to use in catalysts. In addition, Hu and his colleagues[38] deduced that Mo atoms might behave like precious metals in Mo_2C for HER and might well behave as the catalytic active sites. However, the catalytic sites of Mo_2C were difficult to regulate and confirm due to the lack of regular structure.

Herein, we reported a very facile and appealing strategy for synthesizing uniform and ultrathin N-doped Mo_2C nanosheets (N-Mo_2C NSs) using MoO_2 nanosheets (MoO_2 NSs) as a template with special morphology and crystal structure by a rapid, handy, and scalable synthesis, which were utilized as a highly active electrocatalyst for HER. The transformation of the crystal phase and surface atomic structure between MoO_2 NSs and N-Mo_2C NSs is easy to implement due to the ultrathin nanosheet structure. Theoretical calculations validated that the nanosheet structure and N doping of Mo_2C could produce more exposed active sites, including N atoms and Mo atoms on the C plane of Mo_2C. The as-prepared N-Mo_2C NSs displayed noteworthy electrocatalytic activity for HER in both acidic (onset potential of −48.3 mV, Tafel slope of 44.5 mV dec^{-1}) and basic solutions (onset potential of −69 mV, Tafel slope of 65 mV dec^{-1}) with good catalytic and structural stability. Moreover, such a strategy will be able to develop large-scale and high-performance 2D Mo_2C for diverse interesting properties and unusual applications.

RESULTS AND DISCUSSION

Based on prior structural data, β-Mo_2C can be described as a hexagonal-close-packed layer of Mo atoms, with C atoms randomly filling half of the octahedral interstitial sites.[39] A supercell of (4 × 4 × 1) molybdenum carbide and (001) surface was constructed. The different crystal planes exposed

DOI: 10.1021/acsnano.7b06607
ACS Nano 2017, 11, 12509−12518

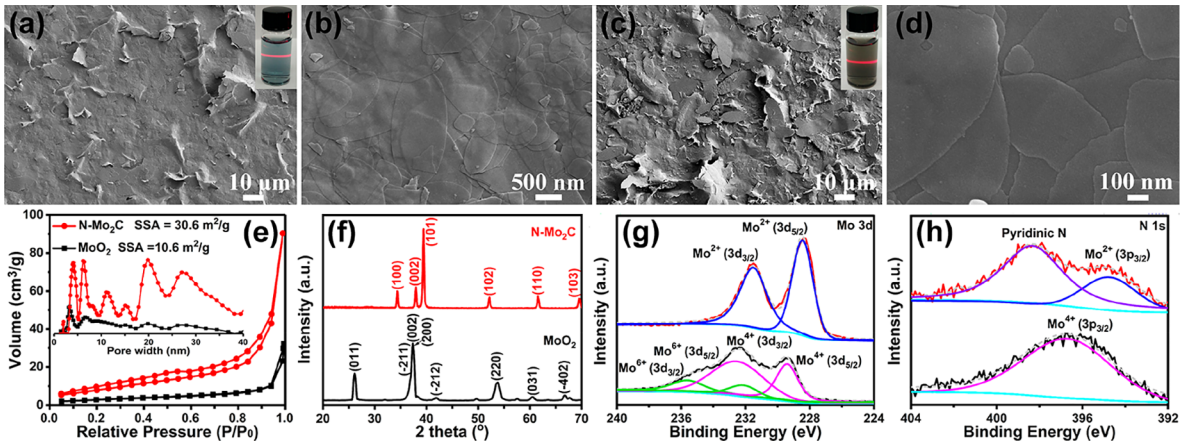

Figure 1. SEM images of (a, b) MoO_2 NSs and (c, d) N-Mo_2C NSs; (e) N_2 adsorption−desorption isotherms and (f) XRD patterns of MoO_2 NSs and N-Mo_2C NS; inset of (e) is the corresponding pore size distributions; XPS spectra of (g) Mo 3d and (h) N 1s of MoO_2 NSs and N-Mo_2C NS. Insets of (a) and (c) are photos of the homogeneous dispersions of MoO_2 NSs and N-Mo_2C NSs in aqueous solution, respectively.

the different atoms, such as Mo atoms on the top plane and C atoms on the bottom plane, as shown in Scheme 1a. The top-view of the C plane and Mo plane of Mo_2C and the detailed distribution of selected points for density functional theory (DFT) are shown in Scheme 1c and Figure S1. DFT calculations were used to calculate the Gibbs free energy of H* adsorption ($|\Delta G_{H^*}|$) on various sites of Mo_2C, such as Mo-1-T, Mo-2-T, and C-T on the top plane and Mo-B on the bottom plane, as shown in Scheme 1d. The $|\Delta G_{H^*}|$ values of Mo-1-T and Mo-2-T on the top plane (0.03 and 0.06 eV) were much lower than those of C-T on the top plane (0.45 eV) and Mo-B on the bottom plane (0.66 eV), implying that Mo atoms on the top plane were mainly catalytically active sites of β-Mo_2C for HER. This was possibly because that Mo-1-T and Mo-2-T atoms on the top plane of Mo_2C were not completely covered by C atoms, which possessed the appropriate hydrogen-binding energy. By contrast, Mo-B atoms on the bottom plane are unsaturated and possessed excessively strong hydrogen-binding energy.

Furthermore, one N atom was introduced into β-Mo_2C to replace one C atom, and the effect of N doping on the ΔG_{H^*} values of Mo and C atoms was studied in Scheme 1b, c, and e. The N doping did not obviously affect the $|\Delta G_{H^*}|$ value of C-T on the top plane (0.4 eV), and even Mo−B on the bottom plane (0.93 eV) became more inert. The catalytically active sites of Mo-1-T (0.03 eV) and Mo-2-T (0.09 eV) atoms on the top plane of Mo_2C remained after N doping. It is important that new catalytically active sites of the N atom and Mo-3-T atom on the top plane were introduced after N doping, which possessed low $|\Delta G_{H^*}|$ values of 0.07 and 0.3 eV, respectively, implying that N doping produced more catalytically active sites of Mo_2C. So, theoretical calculations demonstrated that the Mo atoms on the C plane (top plane) of Mo_2C were more active for HER and the N doping further produced more catalytically active sites, including N atoms and Mo atoms on the C plane (top plane) of Mo_2C.

A nanosheet is a 2D structure with a specific atom alignment that well simplifies the catalysis model as an ideal material model to survey the catalytic sites during HER catalysis. Herein, a two-step process was developed to synthesize the N-Mo_2C NSs, as shown in Figure S2. First, in step a, the regular MoO_2 NSs were obtained by annealing MoO_3 powders in an Ar−H_2 (10% H_2) atmosphere at 900 °C (Figures S3a−d), which were expediently collected at the end of the quartz tube at room temperature on a large scale, such as a synthetic volume for 40 mL with a weight of 1 g (Figure S3e). The equilibrium between sublimation of solid-state MoO_3 and reduction of gaseous MoO_3 by a gas mixture of Ar−H_2 was crucial to synthesize the MoO_2 NSs. Thermal gravimetric analysis-differential scanning calorimetry (TGA-DSC) curves of MoO_3 powders from room temperature to 1000 °C identified the sublimation temperature of MoO_3 at 790 °C (Figure S4). The pure H_2 gas with stronger reduction features used instead of Ar−H_2 only gave large Mo particles (2−4 μm) at the bottom of a porcelain crucible (Figure S5), and no MoO_2 NSs were synthesized on the quartz tube wall. The Ar gas instead of Ar−H_2 was used to synthesize random MoO_3 nanoparticles (2−10 μm), which were collected at the end of the quartz tube (Figure S6). Second, in step b, the N-Mo_2C NSs were synthesized by reacting with dissociative C and N decomposed from dicyandiamide with MoO_2 NSs at 700 °C. The calcination temperatures and dicyandiamide amount can affect the structure, crystalline phase, and according HER activity of molybdenum carbide.

The morphologies of MoO_2 NSs and N-Mo_2C NSs were first examined by scanning electron microscopy (SEM). The resulting MoO_2 NSs exhibited a hexagonal nanosheet-shaped morphology of several micrometers, which possessed a smooth surface and margins (Figure 1a,b). The large-scale SEM image showed the hexagonal nanosheet was evenly distributed (Figure 1a), suggesting the practicability of the synthetic process. After calcination with dicyandiamide at 700 °C, the N-Mo_2C NSs were obtained. As shown in Figure 1c and d, the nanosheets remained, but the surfaces became coarse. The blue and homogeneous aqueous dispersions of MoO_2 NSs and the gray and homogeneous aqueous dispersions N-Mo_2C NSs confirmed the ultrathin 2D structure, which was stable for five months (inset of Figure 1a,c). The specific surface areas of MoO_2 NSs and N-Mo_2C NSs were quantitatively measured using N_2 adsorption−desorption isotherms. As shown in Figure 1e, MoO_2 NSs showed type II, implying the planar structure, confirmed by Langmuir monolayer adsorption. In comparison, N-Mo_2C NSs showed the type IV isotherms with an obvious pore size distribution of 2−40 nm (inset of Figure 1e). The Brunauer−Emmet−Teller (BET) specific surface area of porous N-Mo_2C NSs (30.6 m^2 g^{-1}) was almost tripled from

DOI: 10.1021/acsnano.7b06607
ACS Nano 2017, 11, 12509−12518

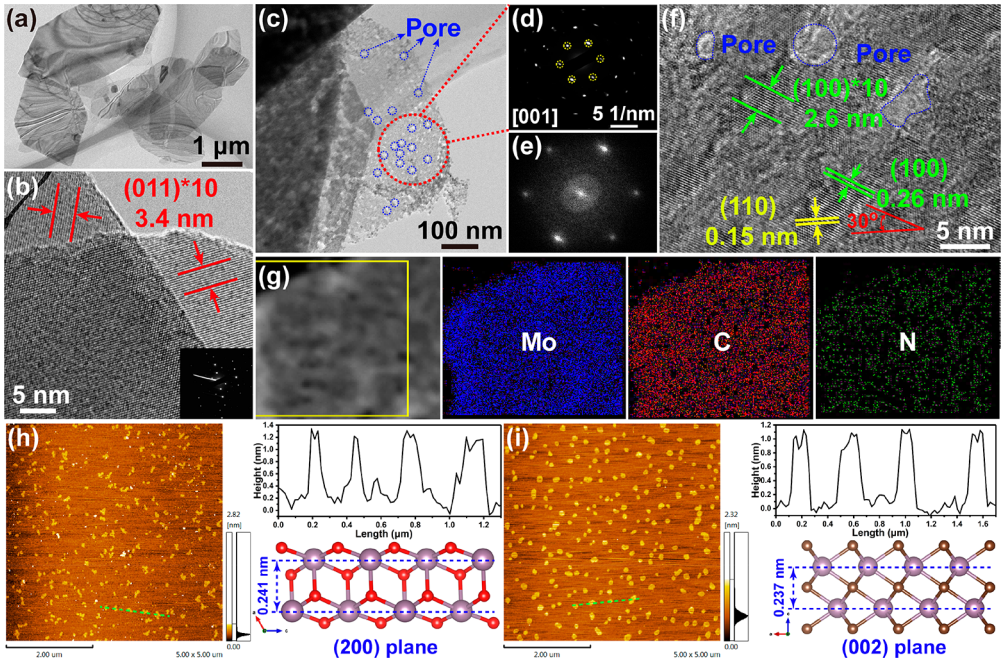

Figure 2. TEM image of (a, b) MoO_2 NSs with corresponding electron-diffraction pattern (inset); TEM image of (c) N-Mo_2C NSs with the corresponding electron diffraction patterns of (d) the single-layer and (e) the fast Fourier transform (FFT, inset) of the hexagonal nanosheets; (f) HRTEM of N-Mo_2C NS; (g) the Mo, C, and N mapping of N-Mo_2C NS. Atomic force microscope (AFM) images (h-1, i-1), thicknesses (h-2, i-2), and crystal models (h-3, i-3) of (h) MoO_2 NSs and (i) N-Mo_2C NSs.

10.6 m^2 g^{-1} of MoO_2 NSs, which was consistent with above SEM results.

X-ray diffraction (XRD) patterns confirmed that the crystal phase transformation from MoO_2 to Mo_2C, which provided proof of a solid-state reaction between the molybdenum and dicyandiamide. As shown in Figure 1f, MoO_2 with monoclinic symmetry crystal structure was obtained (a = 5.611 Å, b = 4.856 Å, c = 5.628 Å, space group $P21/c$ (14), PDF# 73-1249). After reaction with dicyandiamide, the characteristic peaks corresponding to the (100), (002), (101), (102), (110), and (103) crystal facets of the hexagonal β-Mo_2C phase were observed (a = 3.012 Å, b = 3.012 Å, c = 4.735 Å, space group $P63/mm$, PDF# 35-0787). Compared to pure Mo_2C NSs synthesized by glucose, the XRD peaks of N-Mo_2C NSs slightly shifted to a higher diffraction angle (Figure S7). By N doping into the lattice of β-Mo_2C, N-doped β-Mo_2C (100) shifted to a higher angle, indicating that the lattice parameters a/b in β-Mo_2C decreased after N doping into the lattice, which was similar to the doped Mo_2C.[40,41]

The binding states and quantitative chemical compositions of MoO_2 NSs and N-Mo_2C NSs were investigated by X-ray photoelectron spectroscopy (XPS) (Figure 1g, h). The Mo $3d_{3/2}$ and Mo $3d_{5/2}$ of Mo^{4+} were observed at 232.9 and 229.1 eV, and a trace of Mo^{6+} species in an oxidic surrounding was also detected at 235.8 eV (Mo $3d_{3/2}$) and 232.5 eV (Mo $3d_{5/2}$), as a result of the oxidation for a small amount of Mo^{4+} exposed to air (Figure 1g).[42,43] After reaction with dicyandiamide, additional XPS peaks corresponding to N 1s were detected at 398.5 eV (Figure 1h), signifying a successful N doping (17.2 at %) into Mo_2C. The N doping was beneficial to withdraw electrons and active hydrogens caused by the lone electron pair.[44] The main Mo^{2+} with peaks at 228.6 and 231.6 eV (Mo $3d_{5/2}$ and Mo $3d_{3/2}$) was observed in N-Mo_2C NSs (Figure 1g). Compared with that in pure Mo_2C NSs, these shifted peaks for Mo^{2+} in N-Mo_2C NSs with larger binding energy indicated the enriched electrons around Mo (Figure S8), suggesting the successful N doping into Mo_2C NSs.

Transmission electron microscopy (TEM) was applied to further analyze the crystal structure of MoO_2 NSs and N-Mo_2C NSs. Like graphene nanosheets, an obvious wrinkle was observed on the hexagonal MoO_2 NSs, as shown in Figure 2a. Due to ultimately thin shapes, the two pieces of MoO_2 NSs overlaid together, which were transparent to an electron beam. The well-defined lattice fringes with a spacing of 0.34 nm matching with the (011) plane of MoO_2 were observed. The monocrystal nature of the MoO_2 NSs was further proved by the selected area electron diffraction pattern (inset of Figure 2b). After the carbonization and N doping, TEM images further indicated that the morphologies of N-Mo_2C NSs were porous and ultrathin nanosheets (Figures 2c,f and S9). It is worth mentioning that the N-Mo_2C NSs remained hexagonal nanosheets. This was possibly the reason for the small transformation stress of the ultrathin nanosheet structure during the carbonation process. The single set of diffraction spots with 6-fold symmetry clearly indicated the single-crystalline nature and the presence of hexagonal crystalline structures of the nanosheet (Figures 2d,e and S10).[45] The bright lattice fringes shown in Figure 2f indicated that the nanosheets were highly crystallized and porous. A representative HRTEM image clearly showed the long-range order lattice fringes with interplanar spacings of 0.15 and 0.26 nm matching with the (110) and (100) planes of Mo_2C (Figure 2f), respectively. It was confirmed that the crystal orientation [001] was perpendicular to the nanosheet, and the crystal structure of β-Mo_2C situated in the [001] zone axis is shown in Figure S10. As exemplified in Figure 2g, the elemental mapping characterization demonstrated that the nanosheet was evenly comprised of Mo, C, and N elements, confirming the successful synthesis of N-Mo_2C NSs. In addition, the thicknesses of MoO_2 NSs and N-Mo_2C NSs were measured by atomic force microscopy

DOI: 10.1021/acsnano.7b06607
ACS Nano 2017, 11, 12509−12518

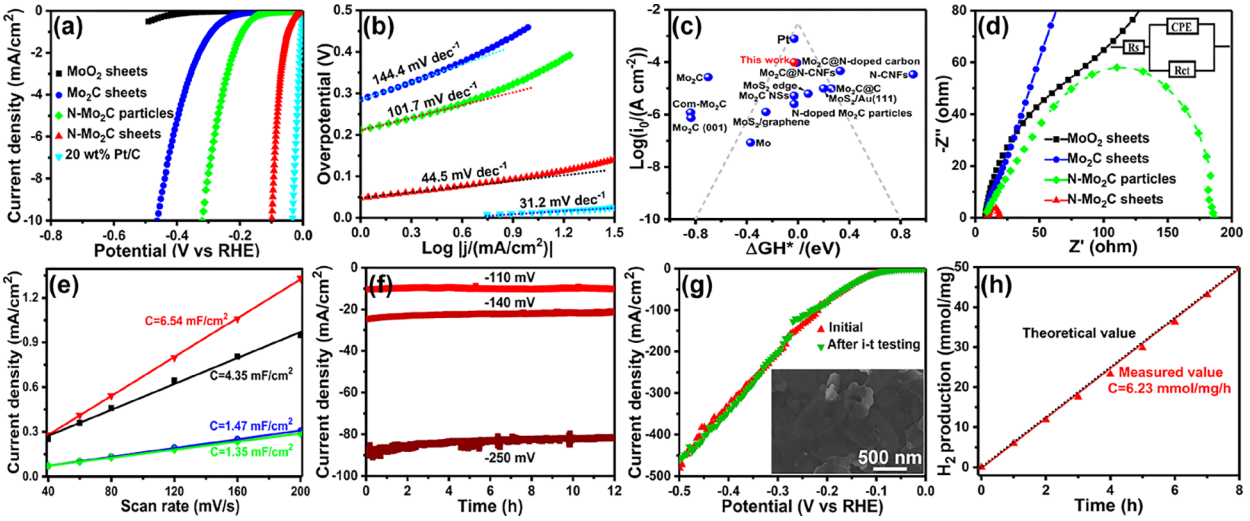

Figure 3. (a) Polarization curves of MoO_2 NSs, Mo_2C NSs, N-Mo_2C nanoparticles, N-Mo_2C NSs, and 20 wt % Pt/C on the GC electrode at 5 mV s^{-1} in 0.5 M H_2SO_4; (b) corresponding Tafel slopes from (a); (c) experimentally measured exchange current, log(i_0), for hydrogen evolution over different metal surfaces plotted as a function of the free energy for hydrogen adsorption, ΔG_{H^*}. All the data come from recent reports.[46−55] (d) Nyquist plots of the different sample-modified electrodes at the same overpotential of 220 mV. Inset is the equivalent circuit; (e) capacitive currents as a function of scan rates; (f) time-dependent current density curves at different overpotentials (110, 140, and 250 mV); (g) polarization curves of N-Mo_2C NSs before and after $i-t$ testing. Inset is the SEM image of the N-Mo_2C NSs after a 12 h $i-t$ testing period. (h) Amount of hydrogen production of porous N-Mo_2C NSs obtained by gas chromatography at different reaction times.

(AFM), as shown in Figure 2h,i. Interestingly, compared with MoO_2 NSs (~1.1 nm, Figures 2h-2 and S11a), the N-Mo_2C NSs obtained *via* carbonization and N doping became slightly thinner (~1.0 nm, Figures 2i-2 and S11b). As confirmed by HRTEM images in Figure 2b and f, the (200) and (002) planes were perpendicular to the MoO_2 NSs and N-Mo_2C NSs, with the interplanar spacings of 0.241 nm (Figure 2h-3) and 0.237 nm (Figure 2i-3), respectively, which caused a thinner nanosheet after the crystalline phase transformation. It is worth noting that MoO_2 NSs and N-Mo_2C NSs were too thin and easily destroyed by ultrasonic dispersion. So, only shapeless sheets with sizes of 0.1−0.2 μm and thicknesses of ~1 nm were observed by AFM.

In order to examine the effect of nanosheet structure and N doping on the HER activity, the blank samples of Mo_2C NSs (Figure S12) and N-Mo_2C nanoparticles with sizes of 0.2−0.4 μm (Figure S13) were synthesized. The electrocatalytic HER performances of the N-Mo_2C NSs and blank samples including MoO_2 NSs, N-Mo_2C nanoparticles, Mo_2C NSs, and 20 wt % Pt/C were evaluated by applying the linear scan voltammogram (LSV) in 0.5 M H_2SO_4 (Figure 3a). The MoO_2 NS-modified electrode showed a large onset potential of >−500 mV *vs* RHE (defined as the potential at 1 mA cm^{-2} of the cathodic current density) for the HER. The N-Mo_2C NSs had the smallest onset potential of −48.3 mV *vs* RHE, much smaller than the value of Mo_2C NSs (−290 mV) and N-Mo_2C nanoparticles (−193 mV), but still worse than that of 20 wt % Pt/C (~0 mV). For running a current density of 10 mA cm^{-2}, N-Mo_2C NSs required an overpotential of only 99 mV, much lower than that observed on the Mo_2C NSs (463 mV) and N-Mo_2C nanoparticles (319.5 mV), indicating that the robust sheet structure and N doping reduced the energy input for activating HER.

Figure 3b displayed the Tafel plots (log $j-\eta$) of the HER. Twenty wt % Pt/C with a Tafel slope of 31.2 mV dec^{-1} followed the known Tafel mechanism. The N-Mo_2C NSs had a smaller Tafel slope of 44.5 mV dec^{-1} than those of Mo_2C NSs (144.4 mV dec^{-1}) and N-Mo_2C nanoparticles (101.7 mV dec^{-1}), signifying that the HER on this catalyst was dominated by the recombination-limited Volmer−Tafel mechanism. The exchange current density (j_0) of the N-Mo_2C NSs was calculated to be 0.1 mA cm^{-2} (Figure S14). This value was much better than that of Mo_2C NSs (5.25×10^{-3} mA cm^{-2}) and N-Mo_2C nanoparticles (2.57×10^{-3} mA cm^{-2}). The established HER free-energy diagram provided a quantitative relationship between the measured electrochemical activity and theoretical ΔG_{H^*} to further evaluate the electrocatalytic properties of the N-Mo_2C NSs in comparison with some typical molybdenum-based electrocatalysts. The normalized experimental value of log(i_0) along with theoretically calculated ΔG_{H^*} was marked on a volcano-shaped plot shown in Figure 3c. It can be seen that the experimental exchange current densities of N-Mo_2C NSs are close to the expected exchange current values in the volcano plot, indicating a good correlation between the theoretical calculation and experimental results. Table S1 summarizes a detailed comparison with other representative molybdenum-based electrocatalysts. Noteworthily, the obtained N-Mo_2C NSs possessed a marvelous HER activity with an onset potential of −48.3 mV *vs* RHE, a Tafel slope of 44.5 mV dec^{-1}, and an overpotential of 99 mV *vs* RHE at 10 mA cm^{-2}, which were obviously better than or comparable to those of the Mo-based HER electrocatalysts in 0.5 M H_2SO_4, such as β-Mo_2C nanotubes (−82 mV, 58 mV dec^{-1}, 136 mV),[30] Mo_2C nanowires (−70 mV, 53 mV dec^{-1}, 200 mV),[25] N, P-Mo_2C@C (~−100 mV, 56 mV dec^{-1}, 141 mV),[56] Mo_2C@N-doped carbon (−60 mV, 60 mV dec^{-1}, 124 mV),[48] Mo_2C/3D N-doped carbon nanofiber (−105 mV, 70 mV dec^{-1}, 192 mV),[46] Mo_2C/hierarchical carbon microflowers (−85 mV, 55 mV dec^{-1}, 144 mV),[27] Mo_2C-carbon sphere (−100 mV, 85 mV dec^{-1}, 164 mV),[57] MoCN nanomaterials (−50 mV, 46 mV dec^{-1}, 140 mV),[22] MoC_x nano-octahedrons (−87 mV, 53 mV dec^{-1}, 142 mV),[34] Mo_2C-WC composite nanowires (~−80 mV, 52 mV dec^{-1}, ~135 mV),[29] Mo_2C/CNT (−63 mV, 65 mV dec^{-1}, 152 mV),[58] Mo_2C/graphitic

DOI: 10.1021/acsnano.7b06607
ACS Nano 2017, 11, 12509−12518

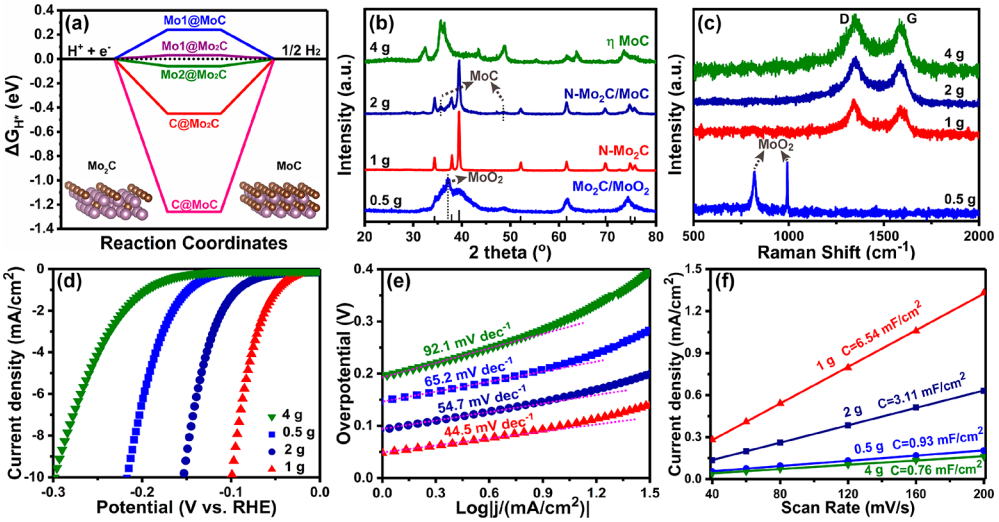

Figure 4. (a) ΔG_{H^*} values of Mo and C atoms in MoC and Mo_2C. Insets are the according theoretical structural models. (b) XRD, (c) Raman spectra, (d) polarization curves, (e) corresponding Tafel slopes, and (f) electrochemical surface area of the samples synthesized with different dicyandiamide amounts.

carbon sheets (−120 mV, 62.6 mV dec^{-1}, 200 mV),[59] Mo_2C/graphene (−87 mV, 73 mV dec^{-1}, 236 mV),[60] *etc.* Furthermore, the N-Mo_2C NSs also had high HER catalytic activities in 1.0 M KOH (onset potential of −69 mV, overpotential of 140 mV, and Tafel slope of 65 mV dec^{-1}) and 1.0 M phosphate-buffered saline (onset potential of −92.5 mV, overpotential of 200 mV, and Tafel slope of 88 mV dec^{-1}) (Figure S15).

To explicate the charge transfer mechanism, electrochemical impedance spectroscopy (EIS) analyses were done on these catalysts as shown in Figure 3d. Clearly, the fitting results confirmed that the lowest resistance (R_s) and charge transfer resistance (R_{ct}) of N-Mo_2C NSs were only 7.5 and 20 Ω at the overpotential of 220 mV, respectively, representing the fastest electrocatalytic reaction rate. The R_{ct} of the N-Mo_2C NSs at overpotentials of 120 and 220 mV showed decreased values from 96 Ω to 20 Ω (Figure S16). At lower overpotentials, *e.g.*, 120 mV, a semicircle could be formed in the Nyquist plots, indicating low charge transfer resistance between the N-Mo_2C NSs and electrolyte.

The strong correlation between the HER catalysis and electrochemical area of N-Mo_2C NSs was accessed by electrochemical double-layer capacitance (Figure 3e). The capacitance of N-Mo_2C NSs (6.54 mF cm^{-2}) was nearly 5 times, 4.4 times, and 1.5 times larger than those of Mo_2C nanoparticles (1.35 mF cm^{-2}), Mo_2C NSs (1.47 mF cm^{-2}), and MoO_2 NSs (4.35 mF cm^{-2}). However, after being corrected by electrochemical area, the HER performance of N-Mo_2C NSs still possessed the lowest onset potential (Figure S17), implying that the larger electrochemical area only increased the number of active sites, but did not enhance the nature of the HER activity. It is worth noting that the cyclic voltammetry (CV) curves of the N-Mo_2C NSs had a nearly rectangular shape (Figure S18), indicating the high electrical conductivity.

The N-Mo_2C NSs exhibited not only great catalytic activity but also good catalytic durability, which was evaluated by time-dependent current (Figure 3f) and LSV after *i*−*t* testing (Figure 3g). The current density of 10 mV cm^{-2} after a 12 h *i*−*t* testing at an overpotential of 110 mV was hardly unchanged. Moreover, the continuous amperometric *i*−*t* testing at large overpotentials of 140 and 250 mV produced large current densities of −20 and −85 mA cm^{-2} for 12 h with negligible attenuations, which meant that N-Mo_2C NSs exhibited good long-term catalytic durability for HER. The almost unchanged polarization curves of N-Mo_2C NSs before and after *i*−*t* testing further confirmed the robust stability (Figure 3g). What is more, the SEM image (inset of Figure 3g), TEM, and XPS spectra (Figures S19) showed that the nanosheet structure was well-preserved and did not show any change of valence states after *i*−*t* testing at 110 mV for 12 h, confirming the structure stability of N-Mo_2C NSs. The residual naphthol was also observed on the surface of nanosheets due to the exfoliation from the glassy carbon electrode. Last, the gathered bubbles on the N-Mo_2C NSs-modified electrode were established to be hydrogen through gas chromatography analysis, and the hydrogen production rate was 6.23 mmol mg^{-1} h^{-1}, which was almost the same as the theoretical calculation (Figure 3h). The obtained Faradaic efficiency (FE) was nearly 100%, implying that N-Mo_2C NSs was an excellent HER electrocatalyst with superior stability in acid media.

The dicyandiamide amount and calcination temperature obviously affected the morphology, phase transformation, and composition of obtained molybdenum carbide and produced different HER activities. Our DFT calculation verified that MoC possessed weaker HER activity than that of Mo_2C due to the oversaturated carbon atoms, as shown in Figure 4a. The ΔG_{H^*} value of the Mo atom of MoC (0.24 eV) was much larger than those of Mo atoms on the C plane of Mo_2C (0.03 and −0.06 eV). In addition, the C atom in MoC (−1.26 eV) was also more inert than that of Mo_2C (−0.45 eV), implying that Mo_2C exhibited a higher HER activity than that of MoC. The dicyandiamide amount affected the crystalline phase and surface structure of molybdenum carbide during the calcining process. The incomplete transformation from MoO_2 NSs to N-Mo_2C NSs was detected with insufficient dicyandiamide (0.5 g, Figure 4b,c). With excess dicyandiamide (4 g), the crystal phase of molybdenum carbide was transformed into η-MoC (PDF# 06-0546), and amorphous carbon at $2\theta \approx 25°$ was detected in Figure 4b. The phase transformation and changed surface structure were also confirmed by the Raman spectra (I_D/I_G, ratio of integrated intensities of D and G bands, Figure 4c) and SEM images (rough surface, Figure S20). With an increasing amount of dicyandiamide, the I_D/I_G value (ratio of integrated

DOI: 10.1021/acsnano.7b06607
ACS Nano 2017, 11, 12509−12518

intensities of D and G bands) increased from 1.4 of 1 g to 2.0 of 2 g and 2.2 of 4 g, showing the increased disordered carbon on the surface of the nanosheets. The polarization curves for HER showed that the N-Mo_2C NSs synthesized with the appropriate amount of dicyandiamide possessed the best HER performance (1 g, Figure 4d,e), which needed not only successfully transformed MoO_2 NSs to N-Mo_2C NSs, but also prevented the phase transformation from Mo_2C to MoC. In addition, the excess carbon on the surface of Mo_2C NSs produced by the more dicyandiamide (Figure 4c) covered the active sites of Mo_2C, which was confirmed by the decreased electrochemical area (Figure 4f).

In addition, the different temperatures (600, 700, 800, and 900 °C) were studied for the influence of N-Mo_2C NSs. At 600 °C, only diffraction peaks of MoO_2 were detected (Figure S21). Because that the dicyandiamide powder was decomposed to ionized molecules of carbon and nitrogen above 700 °C, the low carbonization temperature could not transform MoO_2 NSs into N-Mo_2C NSs. Similar to N-Mo_2C NSs obtained at 700 °C, the samples obtained at 800 °C also possessed the crystal structure of β-Mo_2C and the nanosheet morphology (Figures S21, S22). However, the sheet structure of N-Mo_2C-900 °C began to collapse and formed a lot of nanoparticles due to the high calcination temperature (Figure S21c). Besides, the molybdenum carbide synthesized at 900 °C possessed different crystal phases of η-MoC (space group $\bar{P}m2$, PDF# 06-0546), γ-MoC (space group $P63/mmc$, PDF# 45-1015), and a few β-Mo_2C (space group $P63/mm$, PDF# 35-0787), as shown in Figure S21. The N doping amounts of samples obtained at different temperatures were characterized by XPS in Figure S23a and summarized in Figure S23b. Compared to the N doping amount of 17.2 at. % in N-Mo_2C-700, the increased value (30 at. %) of N-MoO_2-600 was due to the incomplete decomposition of dicyandiamide at low calcination temperatures. Also, the decreased N doping amounts of 8.97 at. % (N-Mo_2C-800) and 6.32 at. % (N-Mo_2C-900) were attributed to the decomposition of the unstable N doping structure at high calcination temperatures. The different phase transformation and composition of N-Mo_2C NSs caused the different HER activity. As shown in Figure S24, the sample obtained at 600 °C possessed the worst HER activity with the onset potential of −200 mV and Tafel slope of 86 mV dec^{-1} due to the unsuccessful transformation from MoO_2 NSs to N-Mo_2C NSs. The β-Mo_2C samples obtained at 700 and 800 °C possessed similar HER activity with onset potential of −48.3 mV (Tafel slope of 44.5 mV dec^{-1}) and −50 mV (Tafel slope of 53 mV dec^{-1}), respectively. The η-MoC/γ-MoC obtained at 900 °C (−103 mV, 62 mV dec^{-1}) possessed the worst HER activity due to the MoC phase (Figures 4a and S21),[25] the collapse of nanosheet structure (Figure S22), decreased N doping amount (Figure S23), and enlarged charge transfer resistance (Figure S25).

CONCLUSIONS

In summary, the N-Mo_2C NSs were fabricated by a two-step approach of using ultrathin MoO_2 NSs as template and a Mo source on a large scale and in a handy way. The obtained N-Mo_2C NSs possessed a single-crystal structure and ultrathin thickness of ∼1.0 nm. Theoretical studies revealed that the 2D structure, N doping, and crystallinity of β-Mo_2C produced more active sites for HER, including exposed Mo atoms on the C plane and N atoms. The as-synthesized N-Mo_2C NSs possessed high HER activity with a low onset potential (−48.3 mV *vs* RHE at 1 mA cm^{-2}), small overpotential (99 mV *vs* RHE at 10 mA cm^{-2}), small Tafel slope (44.5 mV dec^{-1}), high exchange current density (0.1 mA cm^{-2}), and excellent long-term stability (little decay after 12 h *i*−*t* testing). The excellent HER performance of N-Mo_2C NSs was attributed to the following aspects. First, the 2D structure of Mo_2C NSs with large electrochemical area facilitated the diffusion among the electrocatalyst, electrolyte, and gas. Second, the particular crystalline phase and high-proportioned C planes of Mo_2C NSs exposed more Mo active sites (Mo-1-T and Mo-2-T). Third, the synergistic manipulation of N doping with the electron density states produced more active sites (Mo-3-T and N-T). This study provides not only an attractive electrocatalyst with excellent activity toward the HER but also a facile, easy to understand mechanism to optimize Mo-based electrocatalysts for water splitting.

EXPERIMENTAL SECTION

Preparation of N-Doped Mo_2C Nanosheets. The setup is a typical CVD system, which constitutes a clean quartz tube and a tube furnace. First, MoO_2 NSs were grown on the quartz tube tail by a chemical vapor reduction process using commercial MoO_3 powders (99.9%, 0.5 g, Aladdin). The reaction was performed in the presence of mixed Ar−H_2 (10% H_2) gases (200 sccm) at 900 °C for 60 min, and the purple MoO_2 NSs were collected at the tail end of the quartz tube. Second, commercial dicyandiamide powders ($C_2H_4N_4$, 99.99%, 1 g, Aladdin) were mixed with 100 mg of obtained MoO_2 NSs, which were placed in the tube furnace with Ar−H_2 gas to remove air. The mixture was calcined at 450 °C for 2 h and then 700 °C for 2 h to form N-Mo_2C NSs.

For comparison, the pure Mo_2C NSs were made by the same conditions, but with glucose instead of dicyandiamide. The N-doped Mo_2C nanoparticles were also synthesized with MoO_2 nanoparticles and dicyandiamide by the same heating process. Additionally, the calcination temperatures (600, 800, and 900 °C) and amount of dicyandiamide were considered with respect to the effect on the structure and catalytic activities of the samples.

Characterization. Phase compositions of the samples were determined by a D8 Advance X-ray diffractometer (Bruker, Germany) with Cu Kα radiation (λ = 0.154 06 nm). Morphologies of the samples were observed by a field emission scanning electron microscope (MERLIN Compact, Carl Zeiss) and a transmission electron microscope (a JEM-2100F field emission electron microscope, JPN) at an acceleration voltage of 200 kV. The thicknesses of the MoO_2 NSs and N-Mo_2C NSs were analyzed by means of AFM (Dimension Icon, Bruker, Santa Barbara, CA, USA), operated at room temperature and ambient conditions. X-ray photoelectron spectroscopic measurement was implemented with a PHI X-tool instrument (Ulvac-Phi). BET surface areas were determined by using a Quantachrome Autosorb-IQ_2 instrument with nitrogen adsorption at 77 K using the Barrett−Joyner−Halenda method. TGA-DSC curves were measured by a TGA/DSC1 Mettler-Toledo thermal analyzer at a heating rate of 5 °C min^{-1} in a stream of air (50 mL min^{-1}).

Electrochemistry. Electrochemical measurements were operated with an electrochemical workstation (CHI 760C, CH Instruments Inc.) in a 0.5 M H_2SO_4 aqueous solution. An Hg/Hg_2Cl_2 electrode (SCE, saturated KCl aqueous solution) and carbon rod were used as the reference and counter electrodes, respectively. A 5 mg amount of the catalyst powders was dispersed in 1 mL of 2:1 (v/v) water/ethanol mixed solvents along with 40 μL of Nafion solution (∼5% in a mixture of alcohols and water, Sigma-Aldrich) and sonicated for 30 min. Then, 5 μL of the above solution was drop-cast onto the surface of the glassy carbon (GC) electrode at a catalyst loading of 0.357 mg cm^{-2}. The current densities were evaluated in terms of the geometrical surface area of the GC electrode. Polarization curves were acquired by sweeping the potential from 0 to −0.5 V *vs* RHE at a potential sweep rate of 5 mV s^{-1} in 0.5 M H_2SO_4 (pH 0.25), 1.0 M phosphate buffer (pH 7), and 1.0 M KOH (pH 14), which were used as electrolytes,

DOI: 10.1021/acsnano.7b06607
ACS Nano 2017, 11, 12509−12518

individually. EIS was carried out with an amplitude of 0.005 V and a frequency range from 100 kHz to 0.01 Hz. The main arc in each EIS spectrum was fitted using a simplified Randles equivalent circuit, which consisted of a resistance (R_s) in series with a parallel arrangement of a charge transfer resistance (R_{ct}) and a constant phase element, and the fitting parameters were estimated through the application of the Levenberg–Marquardt minimization procedure. Cyclic voltammetry was used to probe the electrochemical double-layer capacitance at nonfaradaic potentials as a means to estimate the effective electrochemical active area. Current–time responses were monitored for 12 h by chronoamperometric measurements. The rate of hydrogen gas production was quantified by gas chromatographic measurements (GC-2060F, Lu Nan Analytical Instruments, LTD, China).

DFT Calculations. In this work, the Gibbs free energy of H atoms on the Mo-terminated and C-terminated (001) surface of Mo_2C was studied using DFT, and the model was established in reference to the work of Wang *et al.*[39] The calculation was performed using VASP (Vienna ab initio simulation package) with the projected augmented-wave method.[61,62] The generalized gradient approximation was used, with exchange correlation following the approach of Perdew–Burke–Ernzerhof.[63] The cutoff energy for the plane-wave basis was set to 520 eV. The Brillouin zone integration was performed on a Γ-centered 5 × 5 × 1 K mesh. All the atoms were fully relaxed until the maximum residual forces of each atom were less than 0.02 eV $Å^{-1}$, the convergence criterion for the self-consistent electronic cycle achieved a difference between the energies of the system in two consecutive steps of smaller than 10^{-5} eV, and the two layers of atoms on the bottom were fixed when hydrogen was absorbed to the surface of Mo_2C. The calculation method for Gibbs free energy followed the widely used method of J. K. Norskov *et al.*[47,64] In addition, the catalytic sites of MoC were also studied using DFT. A 4 × 4 × 2 supercell with a vacuum layer of 15 Å was constructed, and then the (001) facet was cleaved to simulate the surface of MoC. It is worth noting that other sites in structural models of Mo_2C and MoC were considered in our DFT calculation. However, after the structure optimization, H atoms were stably absorbed on the described sites in Figure S1.

ASSOCIATED CONTENT

Supporting Information

The Supporting Information is available free of charge on the ACS Publications website at DOI: 10.1021/acsnano.7b06607.

Top-view and the calculated sites, synthesis process, digital photograph, TGA-DSC, XRD, SEM, XPS, thickness histograms, exchange current density, polarization curves, Tafel slops, Nyquist plots, cyclic voltammograms, and comparison of the HER performance (PDF)

AUTHOR INFORMATION

Corresponding Author

*E-mail: eszhouwj@scut.edu.cn.

ORCID

Hong Liu: 0000-0003-1640-9620

Weijia Zhou: 0000-0003-4339-0435

Notes

The authors declare no competing financial interest.

ACKNOWLEDGMENTS

This work was supported by Tip-top Scientific and Technical Innovative Youth Talents of Guangdong Special Support Program (2016TQ03N541), Guangdong Natural Science Funds for Distinguished Young Scholar (2017B030306001), the National Natural Science Foundation of China (51502096), and Guangdong Innovative and Entrepreneurial Research Team Program (2014ZT05N200).

REFERENCES

(1) Dresselhaus, M.; Thomas, I. Alternative Energy Technologies. *Nature* **2001**, *414*, 332–337.

(2) Koper, M. T. Hydrogen Electrocatalysis: A Basic Solution. *Nat. Chem.* **2013**, *5*, 255–256.

(3) Subbaraman, R.; Tripkovic, D.; Strmcnik, D.; Chang, K. C.; Uchimura, M.; Paulikas, A. P.; Stamenkovic, V.; Markovic, N. M. Enhancing Hydrogen Evolution Activity in Water Splitting by Tailoring Li^+-$Ni(OH)_2$-Pt Interfaces. *Science* **2011**, *334*, 1256–1260.

(4) Yin, H.; Zhao, S.; Zhao, K.; Muqsit, A.; Tang, H.; Chang, L.; Zhao, H.; Gao, Y.; Tang, Z. Ultrathin Platinum Nanowires Grown on Single-Layered Nickel Hydroxide with High Hydrogen Evolution Activity. *Nat. Commun.* **2015**, *6*, 6430.

(5) Cheng, N.; Stambula, S.; Wang, D.; Banis, M. N.; Liu, J.; Riese, A.; Xiao, B.; Li, R.; Sham, T. K.; Liu, L. M. Platinum Single-Atom and Cluster Catalysis of the Hydrogen Evolution Reaction. *Nat. Commun.* **2016**, *7*, 13638.

(6) Li, M.; Ma, Q.; Zi, W.; Liu, X.; Zhu, X.; Liu, S. Pt Monolayer Coating on Complex Network Substrate with High Catalytic Activity for the Hydrogen Evolution Reaction. *Sci. Adv.* **2015**, *1*, e1400268.

(7) Zheng, Y.; Jiao, Y.; Jaroniec, M.; Qiao, S. Z. Advancing the Electrochemistry of the Hydrogen-Evolution Reaction through Combining Experiment and Theory. *Angew. Chem., Int. Ed.* **2015**, *54*, 52–65.

(8) Zhou, W. J.; Jia, J.; Lu, J.; Yang, L. J.; Hou, D. M.; Li, G. Q.; Chen, S. W. Recent Developments of Carbon-Based Electrocatalysts for Hydrogen Evolution Reaction. *Nano Energy* **2016**, *28*, 29–43.

(9) Wang, J.; Cui, W.; Liu, Q.; Xing, Z.; Asiri, A. M.; Sun, X. Recent Progress in Cobalt-Based Heterogeneous Catalysts for Electrochemical Water Splitting. *Adv. Mater.* **2016**, *28*, 215–230.

(10) Shi, Y.; Zhang, B. Recent Advances in Transition Metal Phosphide Nanomaterials: Synthesis and Applications in Hydrogen Evolution Reaction. *Chem. Soc. Rev.* **2016**, *45*, 1529–1541.

(11) Jaramillo, T. F.; Jørgensen, K. P.; Bonde, J.; Nielsen, J. H.; Horch, S.; Chorkendorff, I. Identification of Active Edge Sites for Electrochemical H_2 Evolution from MoS_2 Nanocatalysts. *Science* **2007**, *317*, 100–102.

(12) Chen, W. F.; Sasaki, K.; Ma, C.; Frenkel, A. I.; Marinkovic, N.; Muckerman, J. T.; Zhu, Y.; Adzic, R. R. Hydrogen-Evolution Catalysts Based on Non-Noble Metal Nickel-Molybdenum Nitride Nanosheets. *Angew. Chem., Int. Ed.* **2012**, *51*, 6131–6135.

(13) Wan, C.; Regmi, Y. N.; Leonard, B. M. Multiple Phases of Molybdenum Carbide as Electrocatalysts for the Hydrogen Evolution Reaction. *Angew. Chem.* **2014**, *126*, 6525–6528.

(14) McEnaney, J. M.; Crompton, J. C.; Callejas, J. F.; Popczun, E. J.; Biacchi, A. J.; Lewis, N. S.; Schaak, R. E. Amorphous Molybdenum Phosphide Nanoparticles for Electrocatalytic Hydrogen Evolution. *Chem. Mater.* **2014**, *26*, 4826–4831.

(15) Yang, L.; Zhou, W.; Lu, J.; Hou, D.; Ke, Y.; Li, G.; Tang, Z.; Kang, X.; Chen, S. Hierarchical Spheres Constructed by Defect-Rich MoS_2/Carbon Nanosheets for Efficient Electrocatalytic Hydrogen Evolution. *Nano Energy* **2016**, *22*, 490–498.

(16) Xie, J.; Li, S.; Zhang, X.; Zhang, J.; Wang, R.; Zhang, H.; Pan, B.; Xie, Y. Atomically-Thin Molybdenum Nitride Nanosheets with Exposed Active Surface Sites for Efficient Hydrogen Evolution. *Chem. Sci.* **2014**, *5*, 4615–4620.

(17) Xie, J.; Zhang, J.; Li, S.; Grote, F.; Zhang, X.; Zhang, H.; Wang, R.; Lei, Y.; Pan, B.; Xie, Y. Correction to Controllable Disorder Engineering in Oxygen-Incorporated MoS_2 Ultrathin Nanosheets for Efficient Hydrogen Evolution. *J. Am. Chem. Soc.* **2014**, *136*, 1680–1680.

(18) Jia, J.; Zhou, W.; Li, G.; Yang, L.; Wei, Z.; Cao, L.; Wu, Y.; Zhou, K.; Chen, S. Regulated Synthesis of Mo Sheets and Their Derivative MoX Sheets (X: P, S, or C) as Efficient Electrocatalysts for Hydrogen Evolution Reactions. *ACS Appl. Mater. Interfaces* **2017**, *9*, 8041–8046.

(19) Faber, M. S.; Jin, S. Earth-Abundant Inorganic Electrocatalysts and Their Nanostructures for Energy Conversion Applications. *Energy Environ. Sci.* **2014**, *7*, 3519–3542.

DOI: 10.1021/acsnano.7b06607
ACS Nano 2017, 11, 12509–12518

(20) Chen, W. F.; Iyer, S.; Iyer, S.; Sasaki, K.; Wang, C. H.; Zhu, Y. M.; Muckerman, J. T.; Fujita, E. Biomass-Derived Electrocatalytic Composites for Hydrogen Evolution. *Energy Environ. Sci.* **2013**, *6*, 1818−1826.
(21) Wang, S.; Wang, J.; Zhu, M.; Bao, X.; Xiao, B.; Su, D.; Li, H.; Wang, Y. Molybdenum-Carbide-Modified Nitrogen-Doped Carbon Vesicle Encapsulating Nickel Nanoparticles: A Highly Efficient, Low-Cost Catalyst for Hydrogen Evolution Reaction. *J. Am. Chem. Soc.* **2015**, *137*, 15753−15759.
(22) Zhao, Y.; Kamiya, K.; Hashimoto, K.; Nakanishi, S. *In Situ* CO_2-Emission Assisted Synthesis of Molybdenum Carbonitride Nanomaterial as Hydrogen Evolution Electrocatalyst. *J. Am. Chem. Soc.* **2015**, *137*, 110−113.
(23) Hanif, A.; Xiao, T.; York, A. P.; Sloan, J.; Green, M. L. Study on the Structure and Formation Mechanism of Molybdenum Carbides. *Chem. Mater.* **2002**, *14*, 1009−1015.
(24) Kolel-Veetil, M. K.; Qadri, S. B.; Osofsky, M.; Keller, T. M. Formation of a Superconducting Mixture of β-Mo_2C Nanoparticles and Carbon Nanotubes in an Amorphous Matrix of Molybdenum Compounds by the Pyrolysis of a Molybdenum Derivative of a Carboranylenesiloxane. *Chem. Mater.* **2005**, *17*, 6101−6107.
(25) Liao, L.; Wang, S.; Xiao, J.; Bian, X.; Zhang, Y.; Scanlon, M. D.; Hu, X.; Tang, Y.; Liu, B.; Girault, H. H. A Nanoporous Molybdenum Carbide Nanowire as an Electrocatalyst for Hydrogen Evolution Reaction. *Energy Environ. Sci.* **2014**, *7*, 387−392.
(26) Xu, C.; Wang, L.; Liu, Z.; Chen, L.; Guo, J.; Kang, N.; Ma, X.-L.; Cheng, H.-M.; Ren, W. Large-Area High-Quality 2D Ultrathin Mo_2C Superconducting Crystals. *Nat. Mater.* **2015**, *14*, 1135−1141.
(27) Huang, Y.; Gong, Q.; Song, X.; Feng, K.; Nie, K.; Zhao, F.; Wang, Y.; Zeng, M.; Zhong, J.; Li, Y. Mo_2C Nanoparticles Dispersed on Hierarchical Carbon Microflowers for Efficient Electrocatalytic Hydrogen Evolution. *ACS Nano* **2016**, *10*, 11337−11343.
(28) Lin, H.; Shi, Z.; He, S.; Yu, X.; Wang, S.; Gao, Q.; Tang, Y. Heteronanowires of MoC-Mo_2C as Efficient Electrocatalysts for Hydrogen Evolution Reaction. *Chem. Sci.* **2016**, *7*, 3399−3405.
(29) Xiao, P.; Ge, X.; Wang, H.; Liu, Z.; Fisher, A.; Wang, X. Novel Molybdenum Carbide-Tungsten Carbide Composite Nanowires and Their Electrochemical Activation for Efficient and Stable Hydrogen Evolution. *Adv. Funct. Mater.* **2015**, *25*, 1520−1526.
(30) Ma, F. X.; Wu, H. B.; Xia, B. Y.; Xu, C. Y.; Lou, X. W. D. Hierarchical β-Mo_2C Nanotubes Organized by Ultrathin Nanosheets as a Highly Efficient Electrocatalyst for Hydrogen Production. *Angew. Chem., Int. Ed.* **2015**, *54*, 15395−15399.
(31) Jia, J.; Zhou, W.; Wei, Z.; Xiong, T.; Li, G.; Zhao, L.; Zhang, X.; Liu, H.; Zhou, J.; Chen, S. Molybdenum Carbide on Hierarchical Porous Carbon Synthesized From Cu-MoO_2 as Efficient Electrocatalysts for Electrochemical Hydrogen Generation. *Nano Energy* **2017**, *41*, 749−757.
(32) Seh, Z. W.; Fredrickson, K. D.; Anasori, B.; Kibsgaard, J.; Strickler, A. L.; Lukatskaya, M. R.; Gogotsi, Y.; Jaramillo, T. F.; Vojvodic, A. Two-Dimensional Molybdenum Carbide (MXene) as an Efficient Electrocatalyst for Hydrogen Evolution. *ACS Energy Letters* **2016**, *1*, 589−594.
(33) Ran, J.; Gao, G.; Li, F. T.; Ma, T. Y.; Du, A.; Qiao, S. Z. Ti_3C_2 MXene Co-Catalyst on Metal Sulfide Photo-Absorbers for Enhanced Visible-Light Photocatalytic Hydrogen Production. *Nat. Commun.* **2017**, *8*, 13907.
(34) Wu, H. B.; Xia, B. Y.; Yu, L.; Yu, X. Y.; Lou, X. W. Porous Molybdenum Carbide Nano-Octahedrons Synthesized *via* Confined Carburization in Metal-Organic Frameworks for Efficient Hydrogen Production. *Nat. Commun.* **2015**, *6*, 6512.
(35) Xu, M.; Liang, T.; Shi, M.; Chen, H. Graphene-Like Two-Dimensional Materials. *Chem. Rev.* **2013**, *113*, 3766−3798.
(36) Chhowalla, M.; Jena, D.; Zhang, H. Two-Dimensional Semiconductors for Transistors. *Nat. Rev. Mater.* **2016**, *1*, 16052.
(37) Butler, S. Z.; Hollen, S. M.; Cao, L.; Cui, Y.; Gupta, J. A.; Gutierrez, H. R.; Heinz, T. F.; Hong, S. S.; Huang, J.; Ismach, A. F. Progress, Challenges, and Opportunities in Two-Dimensional Materials Beyond Graphene. *ACS Nano* **2013**, *7*, 2898−2926.
(38) Vrubel, H.; Hu, X. Molybdenum Boride and Carbide Catalyze Hydrogen Evolution in Both Acidic and Basic Solutions. *Angew. Chem., Int. Ed.* **2012**, *51*, 12703−12706.
(39) Wang, T.; Liu, X.; Wang, S.; Huo, C.; Li, Y. W.; Wang, J.; Jiao, H. Stability of β-Mo_2C Facets from *Ab Initio* Atomistic Thermodynamics. *J. Phys. Chem. C* **2011**, *115*, 22360−22368.
(40) Wan, C.; Leonard, B. M. Iron-Doped Molybdenum Carbide Catalyst with High Activity and Stability for the Hydrogen Evolution Reaction. *Chem. Mater.* **2015**, *27*, 4281−4288.
(41) Lin, H.; Liu, N.; Shi, Z.; Guo, Y.; Tang, Y.; Gao, Q. Cobalt-Doping in Molybdenum-Carbide Nanowires Toward Efficient Electrocatalytic Hydrogen Evolution. *Adv. Funct. Mater.* **2016**, *26*, 5590−5598.
(42) Zhao, C.; Yu, C.; Zhang, M.; Huang, H.; Li, S.; Han, X.; Liu, Z.; Yang, J.; Xiao, W.; Liang, J. Ultrafine MoO_2-Carbon Microstructures Enable Ultralong-Life Power-Type Sodium Ion Storage by Enhanced Pseudocapacitance. *Adv. Energy Mater.* **2017**, *7*, 1602880.
(43) Zhu, Y.; Chen, G.; Xu, X.; Yang, G.; Liu, M.; Shao, Z. Enhancing Electrocatalytic Activity for Hydrogen Evolution by Strongly Coupled Molybdenum Nitride@Nitrogen-Doped Carbon Porous Nano-Octahedrons. *ACS Catal.* **2017**, *7*, 3540−3547.
(44) Lu, C. B.; Tranca, D.; Zhang, J.; Hernandez, F. R.; Su, Y. Z.; Zhuang, X. D.; Zhang, F.; Seifert, G.; Feng, X. L. Molybdenum Carbide-Embedded Nitrogen-Doped Porous Carbon Nanosheets as Electrocatalysts for Water Splitting in Alkaline Media. *ACS Nano* **2017**, *11*, 3933−3942.
(45) Dechao, G.; Xiaoxu, Z.; Linjun, L.; Peng, S.; Bingbing, T.; Wei, L.; Jianyi, C.; Dong, S.; Ming, L.; Wu, Z.; Kian Ping, L. Controlled Growth of Ultrathin Mo_2C Superconducting Crystals on Liquid Cu Surface. *2D Mater.* **2017**, *4*, 011012.
(46) Wu, Z. Y.; Hu, B. C.; Wu, P.; Liang, H. W.; Yu, Z. L.; Lin, Y.; Zheng, Y. R.; Li, Z.; Yu, S. H. Mo_2C Nanoparticles Embedded within Bacterial Cellulose-Derived 3D N-Doped Carbon Nanofiber Networks for Efficient Hydrogen Evolution. *NPG Asia Mater.* **2016**, *8*, e288.
(47) Nørskov, J. K.; Bligaard, T.; Logadottir, A.; Kitchin, J.; Chen, J. G.; Pandelov, S.; Stimming, U. Trends in the Exchange Current for Hydrogen Evolution. *J. Electrochem. Soc.* **2005**, *152*, J23−J26.
(48) Liu, Y.; Yu, G.; Li, G. D.; Sun, Y.; Asefa, T.; Chen, W.; Zou, X. Coupling Mo_2C with Nitrogen-Rich Nanocarbon Leads to Efficient Hydrogen-Evolution Electrocatalytic Sites. *Angew. Chem., Int. Ed.* **2015**, *54*, 10752−10757.
(49) Deng, J.; Ren, P.; Deng, D.; Yu, L.; Yang, F.; Bao, X. Highly Active and Durable Non-Precious-Metal Catalysts Encapsulated in Carbon Nanotubes for Hydrogen Evolution Reaction. *Energy Environ. Sci.* **2014**, *7*, 1919−1923.
(50) Shi, Z.; Nie, K.; Shao, Z. J.; Gao, B.; Lin, H.; Zhang, H.; Liu, B.; Wang, Y.; Zhang, Y.; Sun, X. Phosphorus-Mo_2C@Carbon Nanowires Toward Efficient Electrochemical Hydrogen Evolution: Composition, Structural and Electronic Regulation. *Energy Environ. Sci.* **2017**, *10*, 1262−1271.
(51) Fan, X. J.; Liu, Y. Y.; Peng, Z. W.; Zhang, Z. H.; Zhou, H. Q.; Zhang, X. M.; Yakobson, B. I.; Goddard, W. A.; Guo, X.; Hauge, R. H.; Tour, J. M. Atomic H-Induced Mo_2C Hybrid as an Active and Stable Bifunctional Electrocatalyst. *ACS Nano* **2017**, *11*, 384−394.
(52) Tsai, C.; Abild-Pedersen, F.; Nørskov, J. K. Tuning the MoS_2 Edge-Site Activity for Hydrogen Evolution *via* Support Interactions. *Nano Lett.* **2014**, *14*, 1381−1387.
(53) Merki, D.; Vrubel, H.; Rovelli, L.; Fierro, S.; Hu, X. Fe, Co, and Ni Ions Promote the Catalytic Activity of Amorphous Molybdenum Sulfide Films for Hydrogen Evolution. *Chem. Sci.* **2012**, *3*, 2515−2525.
(54) Morales-Guio, C. G.; Stern, L. A.; Hu, X. Nanostructured Hydrotreating Catalysts for Electrochemical Hydrogen Evolution. *Chem. Soc. Rev.* **2014**, *43*, 6555−6569.
(55) Hu, J.; Huang, B.; Zhang, C.; Wang, Z.; An, Y.; Zhou, D.; Lin, H.; Leung, M. K.; Yang, S. Engineering Stepped Edge Surface Structures of MoS_2 Sheet Stacks to Accelerate the Hydrogen Evolution Reaction. *Energy Environ. Sci.* **2017**, *10*, 593−603.
(56) Chen, Y. Y.; Zhang, Y.; Jiang, W. J.; Zhang, X.; Dai, Z.; Wan, L. J.; Hu, J. S. Pomegranate-Like N, P-Doped Mo_2C@C Nanospheres as

DOI: 10.1021/acsnano.7b06607
ACS Nano 2017, 11, 12509−12518

Highly Active Electrocatalysts for Alkaline Hydrogen Evolution. *ACS Nano* **2016**, *10*, 8851−8860.
(57) Wu, Z.; Wang, J.; Liu, R.; Xia, K.; Xuan, C.; Guo, J.; Lei, W.; Wang, D. Facile Preparation of Oarbon Sphere Supported Molybdenum Compounds (P, C and S) as Hydrogen Evolution Electrocatalysts in Acid and Alkaline Electrolytes. *Nano Energy* **2017**, *32*, 511−519.
(58) Chen, W. F.; Wang, C. H.; Sasaki, K.; Marinkovic, N.; Xu, W.; Muckerman, J. T.; Zhu, Y.; Adzic, R. R. Highly Active and Durable Nanostructured Molybdenum Carbide Electrocatalysts for Hydrogen Production. *Energy Environ. Sci.* **2013**, *6*, 943−951.
(59) Cui, W.; Cheng, N.; Liu, Q.; Ge, C.; Asiri, A. M.; Sun, X. Mo_2C Nanoparticles Decorated Graphitic Carbon Sheets: Biopolymer-Derived Solid-State Synthesis and Application as an Efficient Electrocatalyst for Hydrogen Generation. *ACS Catal.* **2014**, *4*, 2658−2661.
(60) Geng, D.; Zhao, X.; Chen, Z.; Sun, W.; Fu, W.; Chen, J.; Liu, W.; Zhou, W.; Loh, K. P. Direct Synthesis of Large-Area 2D Mo_2C on *In Situ* Grown Graphene. *Adv. Mater.* **2017**, *29*, 1700072.
(61) Blöchl, P. E. Projector Augmented-Wave Method. *Phys. Rev. B: Condens. Matter Mater. Phys.* **1994**, *50*, 17953.
(62) Kresse, G.; Joubert, D. From Ultrasoft Pseudopotentials to the Projector Augmented-Wave Method. *Phys. Rev. B: Condens. Matter Mater. Phys.* **1999**, *59*, 1758.
(63) Perdew, J. P.; Burke, K.; Ernzerhof, M. Generalized Gradient Approximation Made Simple. *Phys. Rev. Lett.* **1996**, *77*, 3865.
(64) Jiao, Y.; Zheng, Y.; Davey, K.; Qiao, S. Z. Activity Origin and Catalyst Design Principles for Electrocatalytic Hydrogen Evolution on Heteroatom-Doped Graphene. *Nature Energy* **2016**, *1*, 16130.

DOI: 10.1021/acsnano.7b06607
ACS Nano 2017, 11, 12509−12518